THE SDSS COADD: COSMIC SHEAR MEASUREMENT

Huan Lin[1], Scott Dodelson[1,2,3], Hee-Jong Seo[4], Marcelle Soares-Santos[1], James Annis[1], Jiangang Hao[1], David Johnston[1], Jeffrey M. Kubo[1], Ribamar R. R. Reis[1,5], Melanie Simet[2,3]
[1]Center for Particle Astrophysics, Fermi National Accelerator Laboratory, Batavia, IL 60510
[2]Department of Astronomy & Astrophysics, The University of Chicago, Chicago, IL 60637
[3]Kavli Institute for Cosmological Physics, Chicago, IL 60637
[4]Berkeley Center for Cosmological Physics, LBL and Department of Physics, University of California, Berkeley, CA, USA 94720
[5]Instituto de Física, Universidade Federal do Rio de Janeiro, CEP 21941-972, Rio de Janeiro, RJ, Brazil

Draft version December 21, 2011

ABSTRACT

Stripe 82 in the Sloan Digital Sky Survey was observed multiple times, allowing deeper images to be constructed by coadding the data. Here we analyze the ellipticities of background galaxies in this 275 square degree region, searching for evidence of distortions due to cosmic shear. The E-mode is detected in both real and Fourier space with > 5-σ significance on degree scales, while the B-mode is consistent with zero as expected. The amplitude of the signal constrains the combination of the matter density Ω_m and fluctuation amplitude σ_8 to be $\Omega_m^{0.7}\sigma_8 = 0.252^{+0.032}_{-0.052}$.

Subject headings: cosmological parameters — cosmology: observations — gravitational lensing — large-scale structure of universe

1. INTRODUCTION

Since the first detections of cosmic shear (Van Waerbeke et al. 2000; Bacon et al. 2000; Wittman et al. 2000), gravitational lensing has emerged as a powerful tool in the quest to pin down cosmological parameters (Rhodes et al. 2001; Van Waerbeke et al. 2001; Hoekstra et al. 2002; Jarvis et al. 2003; Bacon et al. 2003; Hamana et al. 2003; Heymans et al. 2004; Rhodes et al. 2004; Fu et al. 2008; Schrabback et al. 2010). Distortions in the shapes of distant galaxies depend on the intervening cosmic shear field, and careful observations of the ellipticities of many background galaxies enable us to measure the statistics of this field, and compare with the predictions of a given cosmological model. This comparison is most robust on large scales, which are unaffected by non-linearities and baryonic effects. However, observations are easiest on the small scales covered by deep surveys where the point spread function is relatively stable, so only recently have detections moved to larger scales. Indeed, one of the most promising applications of weak lensing is to measure properties of dark energy (see Munshi et al. 2008, for a review), and for this purpose, precise measurements on scales of order ten arcminutes and larger will be most constraining.

With this in mind, we have measured the ellipticities of galaxies in Stripe 82 of the Sloan Digital Sky Survey (SDSS; York et al. 2000), a rectangular ($2.5° \times 110°$) region on the sky that was imaged multiple times. The images have been coadded leading to a much deeper picture of the galaxies in the Universe than is available from the part of the survey comprised of single images (Annis et al. 2011). The relatively large area and deep images offer a glimpse into the future, as large scale surveys such as the Dark Energy Survey (DES; Abbott et al. 2005) and the Large Synoptic Survey Telescope (LSST; Abell et al. 2009) come on line. As we present results obtained on the coadded data, an important considera-

tion is the systematics associated with the coadd. How careful must one be when combining multiple images of the sky?

Section 2 describes the data set, the coaddition method, the correction for the effects of the point spread function (PSF) modeling, and the prescription for obtaining photometric redshifts. Section 3 reviews the different two-point functions used to characterize the shear distribution and how these are related to the underlying matter power spectrum. Section 4 presents the correlation function results for both mock catalogs (to obtain a benchmark against which the actual data can be compared) and the data. Section 5 presents a complementary approach by estimating the Fourier space power spectrum in several different ways. In each case (real space with the correlation function and Fourier space with the power spectrum), we isolate modes that should be non-zero and modes that arise due to systematics and show that the former are detected and the latter are consistent with zero. Finally, in Section 6 we use the two-point function results to obtain constraints on the fluctuation amplitude σ_8 and matter density Ω_m. Section 7 summarizes our results and conclusions.

While this work was underway, we learned of a parallel effort by Huff et al. (2011). These two efforts use different methods of coaddition and different sets of cuts for the input images and galaxies; what they have in common is their use of SDSS data (not necessarily the same set of runs) and their use of the SDSS PHOTO pipeline for the initial reduction of the single epoch data and the final reduction of the coadded data (however, they use different versions of PHOTO). Using these different methods, both groups have attempted to extract the cosmic shear signal and its cosmological interpretations. We have coordinated submission with them but have not consulted their results prior to this, so these two analysis efforts are completely independent, representing an extreme version of two independent pipelines.

2. STRIPE 82 COADD DATA

2.1. *Coadd*

The SDSS (York et al. 2000) obtained CCD imaging in five bands over 10,000 square degrees in the Northern Galactic Cap. In addition, the SDSS imaged the Celestial Equator in the Southern Galactic Cap (Stripe 82) multiple times during the Fall months when the Northern Cap was not observable. The SDSS Coadd (Annis et al. 2011) is a 275 square degree survey resulting from the stacking of 20-30 exposures on Stripe 82. The depth achieved is 2 magnitudes fainter and the seeing is $0.3''$ better than the SDSS Northern Cap data, which is comprised of single exposures. Annis et al. (2011) provides a detailed description of the coadd construction process and the resulting data set, which includes images and catalogs, all publicly available as part of the SDSS Data Release 7 (Abazajian et al. 2009). Here we summarize the relevant aspects for this work.

SDSS imaging is obtained in a time-delay-and-integrate (or drift scan) mode in five filters $ugriz$ (Fukugita et al. 1996) using the 2.5 degree wide SDSS imaging camera (Gunn et al. 1998). The coadd area is, therefore, 2.5 degree wide and covers the range $-50 \leq$ RA ≤ 60 degrees on Stripe 82. For most of the program images were taken under photometric conditions and good seeing, but the SDSS Supernova program took data in the same area even under non-photometric conditions when the seeing was poor.

Although Stripe 82 has been imaged more than 100 times, the number of exposures included in the coadd is 20-30 because the data were selected using various quality criteria and, at the time of processing, only data up to December 1 2005 were available. Fields were selected based on r-band parameters. In addition to the basic requirement that the fields contain enough stars for relative calibration, the selection allowed at the most $2''$ PSF FWHM, 0.5 mag of sky noise increase and 0.2 mag of extinction. Rejection of entire fields based on r-band parameters maximizes the homogeneity of the input data for the coadd construction.

The selected fields undergo photometric calibration and sky subtraction. Masks accounting for Stripe 82 geometry and bad/saturated pixels are created as well as the inverse variance and weight maps. All images, maps and masks are aligned on a rectangular grid with the appropriate dimensions ($-50° \leq$ RA $\leq 60°$ and $-1.25° \leq$ Dec $\leq 1.25°$) and in the usual SDSS image format (1489 rows along RA and 2048 columns along Dec, at $0.396''$/pix scale in a J2000 coordinate system).

The coaddition itself is done using a weighted clipped mean on an image by image basis where $w_i = T_i/(\sigma_i \times \mathrm{FWHM}_i)^2$ is the weight and T_i, σ_i and FWHM_i are the sky transparency, sky noise and seeing of the ith image. Good seeing data taken when the sky is clear and the atmospheric glow is at a minimum are weighted higher by this scheme, which reduces the average PSF in the coadd images to $1.1''$ (median seeing for the SDSS single exposure data is $1.4''$). The PSFs in the Coadd were obtained by adding the input PSFs using the same weights used for the images. The resulting PSF was used as input to the SDSS photometric pipeline (PHOTO, Lupton et al. (2001)) which produces the galaxy catalog used as base for this work. The quantities listed in the catalog are the same quantities reported for the SDSS main survey catalog, including measurements of the second and fourth moments for each galaxy and of the PSF at the position of each galaxy.

2.2. *Photometric redshifts*

Photometric redshifts are crucial for this work, as well as related projects. A neural network algorithm that was successfully used in the SDSS DR6 (Oyaizu et al. 2008b) was applied to the coadd galaxies. The resulting photometric redshift galaxy catalog is fully described in Reis et al. (2011) and is publicly available as an SDSS DR7 value-added catalog. Here we present an overview of the method and the catalog properties that are relevant for this work.

We use a particular type of Adaptive Neural Network called Feed Forward Multilayer Perceptron (FFMP) to map the relationship between photometric observables and redshifts (for details see Reis et al. 2011; Oyaizu et al. 2008b). An FFMP network consists of several input nodes, one or more hidden layers, and several output nodes, all interconnected by weighted connections. Once the network configuration is specified, it can be trained to output an estimate of redshift given the input photometric observables. The training process involves finding the set of weights that gives the best photometric redshift estimate for the training set (a sample of galaxies with spectroscopic redshifts). These weights are then applied to the full photometric sample to produce a photometric redshift catalog. Errors are estimated using the Nearest Neighbor Error estimator (Oyaizu et al. 2008a). This estimator associates photo-z errors to photometric objects by considering the errors for objects with similar multi-band magnitudes in the validation set (a second sample of galaxies with spectroscopic redshifts).

A spectroscopic sample of $82,741$ galaxies was established by gathering data from various surveys overlapping Stripe 82. 69% of the sample was obtained from the SDSS data (Abazajian et al. 2009), 12% from DEEP2 (Weiner et al. 2005), 11% from WiggleZ (Drinkwater et al. 2010), 7% from VVDS (Garilli et al. 2008), and 2% from CNOC2 (Yee et al. 2000). The full sample is divided in two sets of equal size, for training and validation respectively. The best results are obtained when magnitudes are used as input parameters and the training is performed in independent magnitude slices in the r-band.

The resulting galaxy catalog, with photometric redshift measurements, forms the base catalog for this work. The photometric redshifts are well measured up to $z \sim 0.8$, the mean photo-z error of the validation set galaxies is $\sigma_z = 0.031$, and the average estimated photo-z error for the full sample is $\sigma_z = 0.18$. Our analysis relies on the redshift probability distribution function of the galaxies used in the cosmic shear measurement. As discussed in the following section, we perform several cuts in the galaxy catalog to mitigate the systematic effects. We cut in i-band magnitude ($18 < i < 24$), size ($> 1.5\times$ the PSF size) and ellipticity components (< 1.4). The overall photometric redshift distribution, for the galaxies remaining after these cuts is shown in Fig. 1 (grey histogram). Motivated by the fact that the photometric redshift distribution is also a source of systematics in

our analyses, and that we observe a narrow peak in the distribution at $z \sim 0.8$ due to large errors at high z, we tested two cuts in photometric redshift errors, $\sigma_z < 0.20$ and $\sigma_z < 0.15$. These are also shown in Fig. 1 (blue and red histograms, respectively) and the corresponding results will be discussed in the following sections.
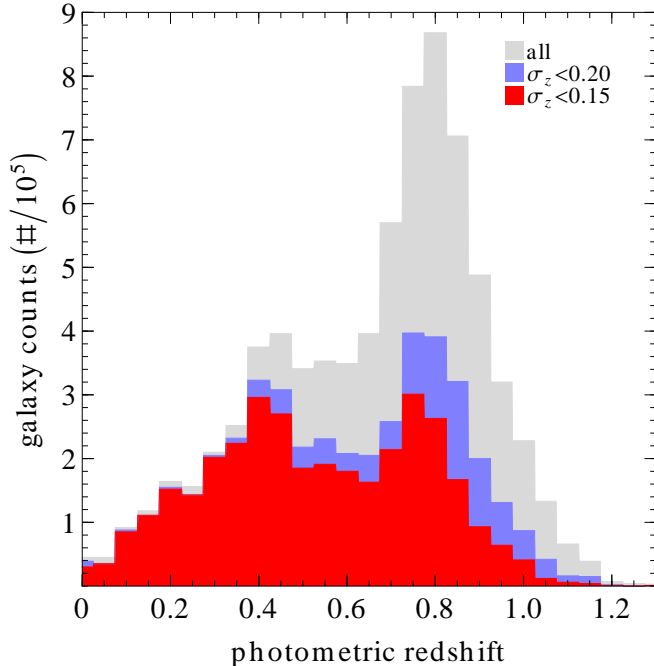

FIG. 1.— Photometric redshift distribution for galaxies passing the magnitude, size and ellipticity cuts (grey) and the photometric redshift error cuts $\sigma_z < 0.20$ (blue) and $\sigma_z < 0.15$ (red).

2.3. Shape Measurement and PSF Correction

The initial shape measurement is performed using the SDSS `PHOTO` pipeline (Lupton et al. 2001), which measures the shapes of objects using adaptive moments (Bernstein & Jarvis 2002). However, we find that we need to correct the point spread function (PSF) model computed by the SDSS reduction pipeline, as there are small but significant systematic offsets between the PSF model adaptive moments and the same quantities as directly measured on bright stars. For example, the top panel of Fig. 2 shows the residuals in the ellipticity component e_1, relative to the PSF model, for unsaturated bright stars with $16 < i < 17$. Note that our e_1, e_2 convention is such that the positive x and y directions are aligned along the positive Dec and RA directions, respectively. The e_1 residuals show a small overall bias ($\Delta e_1 = 0.004$), as well as conspicuous trends ($\Delta e_1 \sim 0.01$) as a function of declination, plus discontinuities between neighboring CCD camera columns ("camcols"). Note there are 12 camcols in all: 6 physical columns of CCDs in the SDSS imaging camera, which are then interleaved by the North and South scans of Stripe 82. In order to remove these PSF residuals, which would otherwise contribute systematic errors to the cosmic shear measurements, we make corrections to the PSF model by fitting polynomials to the residuals along the declination direction, separately for each of the 12

camcols, and for each of the 4 adaptive moments quantities relevant to the linear PSF correction scheme we will use (Appendix B of Hirata & Seljak 2003). Specifically, we fit quadratic polynomials in declination to the residuals in the two ellipticity components (`mE1-mE1PSF`, `mE2-mE2PSF`) and in the size (`mRrCc - mRrCcPSF`), and we fit linear polynomials to the residuals in the 4th moment (`mCr4 - mCr4PSF`). The bottom panel of Fig. 2 shows the improved e_1 residuals after applying the correction procedure of subtracting off the best-fit polynomial to the original e_1 residuals vs. declination. The improvement in the residuals is visible, for example, at declination $\approx -1°$, at the boundary between the first two camcols: the discontinuity visible there in the top panel is gone in the bottom panel, after the application of our correction procedure.
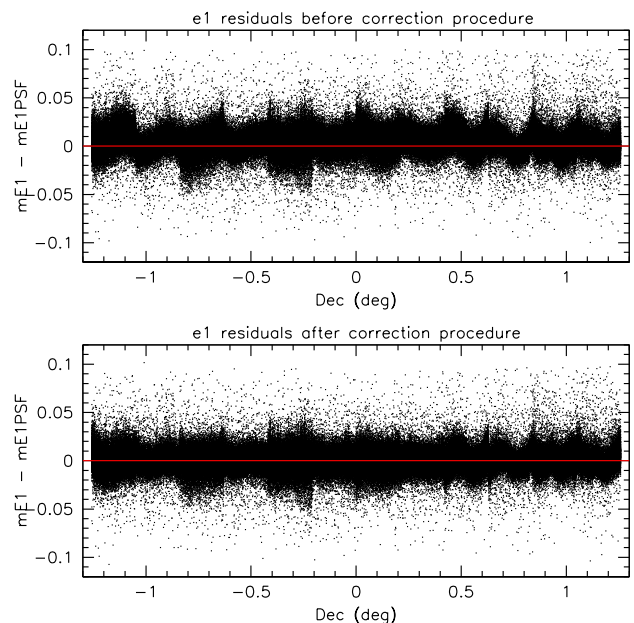

FIG. 2.— *Top panel:* The difference between the measured ellipticity component e_1 and the PSF model e_1, for unsaturated bright stars with $16 < i < 17$, plotted against declination. Note the small overall bias and the trends and discontinuities in these e_1 residuals. *Bottom panel:* Same as the top but after applying the PSF correction procedure described in the text, which removes the bias, as well as reduces the trends and discontinuities in the e_1 residuals.

After correcting the PSF model as described above, we proceed to calculate PSF-corrected galaxy ellipticities, using the linear PSF correction algorithm described in Hirata & Seljak (2003). The galaxies used in our lensing analysis are required to be classified by `PHOTO` as galaxies (type=3), have extinction corrected model magnitudes (Stoughton et al. 2002) in the range $18 < i < 24$, not contain saturated pixels, and not have flags indicating problems with the adaptive moments measurements. We use only the shape measurements from the i band as it is the filter that has the best seeing ($1.05''$) in the coadd, as shown in Annis et al. (2011). Similar to Mandelbaum et al. (2005), we use the `PHOTO` star/galaxy classification and restrict the sample to galaxies at least 50% larger than the PSF. This is quantified by requir-

ing the *resolution factor* R > 0.33, where R (not to be confused with responsivity R introduced below) is given by

$$R = 1 - \frac{M_{\mathrm{rrcc}}^{\mathrm{PSF}}}{M_{\mathrm{rrcc}}} \qquad (1)$$

where M_{rrcc} and $M_{\mathrm{rrcc}}^{\mathrm{PSF}}$ are the sum of the second order moments (in the CCD row and column directions) of the object and PSF respectively. Similar to the SDSS lensing analysis of Hirata et al. (2004), we further restrict the galaxies used in our study to those with PSF-corrected ellipticities $|e_1| < 1.4$ and $|e_2| < 1.4$. The number of galaxies used in our analysis is 3.70 million for the photo-z error $\sigma_z < 0.15$ sample and 4.69 million for the $\sigma_z < 0.2$ sample. These numbers correspond to surface densities of 3.7 and 4.7 galaxies per arcmin^2, respectively. The rms ellipticity for our galaxies is $\sigma_e = 0.44$ (for each of the e_1 and e_2 components) for the $\sigma_z < 0.15$ sample and $\sigma_e = 0.47$ for the $\sigma_z < 0.2$ sample. Note that σ_e^2 is effectively the average value of the quadrature sum of the intrinsic shape noise and the ellipticity measurement error (and a small contribution from the cosmic shear signal) for each galaxy. Following Hirata et al. (2004), the intrinsic shape noise contribution alone is $e_{\mathrm{int}} = 0.37$ per ellipticity component, resulting in a shear responsivity $R = 2(1 - e_{\mathrm{int}}^2) = 1.7$. We then convert from ellipticity to shear γ using $\gamma = e/R$.

We have found that the PSF-corrected galaxy ellipticities e_1 and e_2 have typical average values over each CCD camcol of $|\bar{e}_1|$, $|\bar{e}_2| \approx 0.003$, whereas we would have expected that the average over a thin but very long $\sim 0.2°$ by 110° camcol should be closer to zero, i.e., $|\bar{e}| \approx 8 \times 10^{-4}$, given the measured rms ellipticity $\sigma_e = 0.45$ and the average of 3.5×10^5 galaxies per camcol. We have attributed this additive bias in the ellipticity measurements to remaining camcol-dependent systematic errors in our PSF model, and have chosen to correct for the bias by subtracting off the mean of the galaxy e_1 and e_2 values on a camcol-by-camcol basis. If not corrected, the result is to cause additive offsets in the correlation function ξ of order $|\Delta\xi| \sim \bar{e}^2/R^2 \sim 3 \times 10^{-6}$, comparable to the cosmic shear signal we will measure in Section 4.2. In Section 4.3 we will assess the potential impact on our lensing analysis of any residual systematic effects due to the PSF, by checking the cross correlation function of the PSF and galaxy ellipticities.

Next, we divide the Stripe 82 area into square pixels of size $0.1° \times 0.1°$, and compute the average PSF-corrected ellipticity components e_1 and e_2 in each pixel for all the galaxies meeting our lensing sample criteria. We use these averaged ellipticity values in our subsequent analyses. Fig. 3 shows an example map of galaxy ellipticities for a small part of the Stripe 82 area. The map is shown both before and after PSF correction, in particular illustrating the efficacy in removing the PSF-induced ellipticity patterns in the outer CCD camera columns, along the top of Fig. 3. The distributions over our full data area of the pixel-averaged e_1 and e_2 values are plotted in Fig. 4, both before and after PSF correction. The pre-corrected galaxy ellipticity distributions clearly show the effects of the PSF. In particular, the main feature is the negative mean and tail seen in the e_1 distribution, indicating an elongation of the galaxy shapes along the RA direction, which is also the scan direction of the coadd

imaging runs. In contrast, after applying the PSF correction procedure as described above, the galaxy ellipticity distributions are seen to be much better behaved, without any conspicuous asymmetry or bias. In fact, the post-correction e_1 and e_2 distributions are each well approximated by a Gaussian with $\sigma \approx 0.04$. This value of σ is consistent with the single-galaxy rms ellipticity, $\sigma_e = 0.45$, divided by the square root of the average number of galaxies per pixel $\bar{N}$, where $\bar{N} = 129$ and 163 for the $\sigma_z < 0.15$ and 0.20 samples, respectively.

3. TWO-POINT FUNCTIONS

The measured ellipticities, e_1 and e_2, receive contributions (in addition to the noise) from the cosmic shear components γ_1 and γ_2. The mean cosmic shear is zero, but the correlations are non-zero and dictated by the underlying cosmology. The most basic two-point function is obtained by multiplying the shears (e_i/R) of pairs of galaxies, collecting pairs with angular separations in a given bin to form, e.g., $\xi_{ii}(\theta)$. This two point function depends on the power spectrum of the convergence field κ; for example, the expected value of the correlation function for γ_1 between two pixels located at angular positions $\vec{n}_1$ and $\vec{n}_2$ is (Hu & White 2001)

$$\langle \gamma_1(\vec{n}_1)\gamma_1(\vec{n}_2)\rangle = \int \frac{d^2 l}{(2\pi)^2} C_l^{EE} \cos^2 2\varphi_l$$
$$\times \left[j_0(l_x\sigma/2) j_0(l_y\sigma/2) \right]^2 e^{i\vec{l}\cdot(\vec{n}_1 - \vec{n}_2)} \quad (2)$$

where φ_l is the angle that the 2D vector $\vec{l}$ makes with a fixed x-axis and the spherical Bessel functions encode the effects of the window function of a square pixel with sides σ. The power spectrum of the convergence is

$$C_l^{EE} = \int_0^\infty d\chi \frac{W^2(\chi)}{\chi^2} P_\delta(k = l/\chi; z(\chi)). \qquad (3)$$

where $\chi(z)$ is the comoving distance out to redshift z, P_δ is the matter power spectrum, and the window function depends on the distribution of background galaxies:

$$W(\chi) = \frac{3}{2}\Omega_m H_0^2 \chi \int_\chi^\infty d\chi' \frac{dn}{d\chi'} \left(1 - \frac{\chi}{\chi'} \right) \qquad (4)$$

with H_0 the current Hubble rate. For the redshift distribution of Stripe 82, the window function is a smooth function peaking at $z \simeq 0.35$ and is shown in Fig. 5.

Note that the 2-point function of γ_1 in Eq. (2) depends not only on the angular distance between two pixels, but also on the direction of this vector $\vec{n}_1 - \vec{n}_2$. It is therefore useful to combine the various 2-point functions of γ_1 and γ_2 into two that depend only on the distance, one of which is not sourced by the convergence and so should vanish, and the other of which contains all the information about the power spectrum of the convergence. Towards this end, we decompose the shears into tangential and cross components measured relative to the line connecting a galaxy pair. The tangential component is perpendicular (positive) or parallel (negative) to this line, while the cross-component has axes 45 and 135 degrees away from this line. The correlation function of the two components are then built by summing the products of $e_t e_t$ and $e_\times e_\times$ for each pair separated by an angular distance within the bin of interest. One can then show that, of the two linear combinations

$$\xi_\pm(\theta) \equiv \xi_{tt}(\theta) \pm \xi_{\times\times}(\theta), \qquad (5)$$
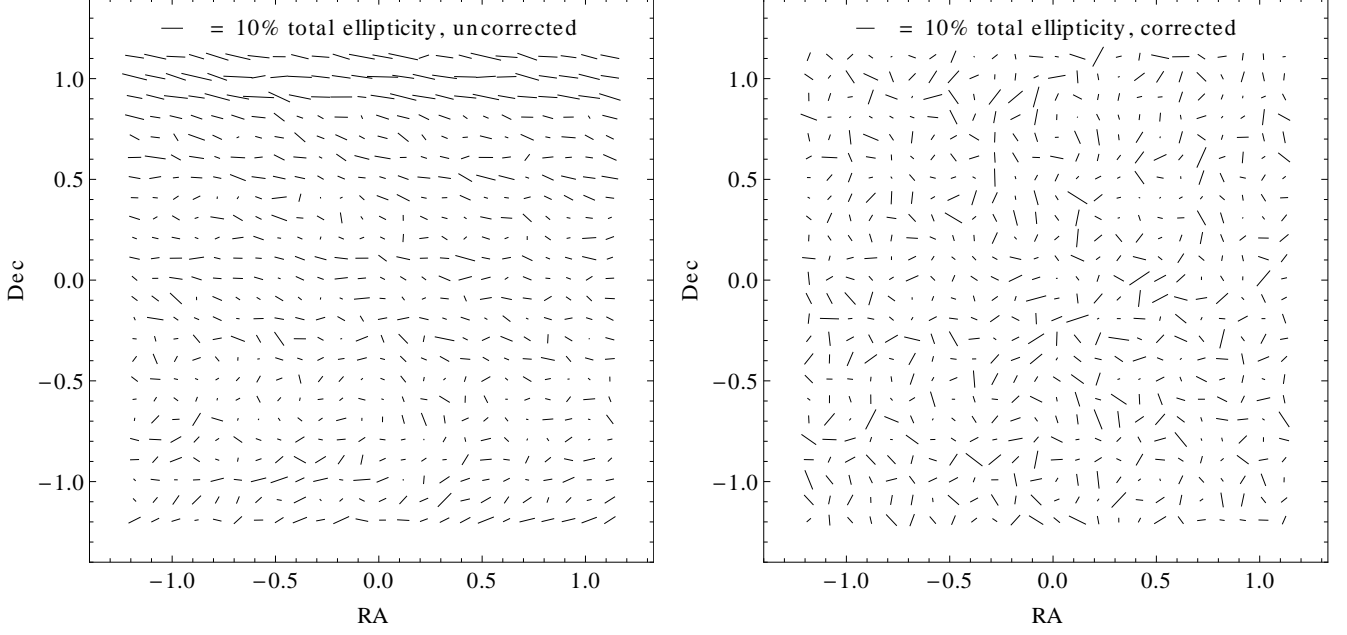
FIG. 3.— Map of the galaxy ellipticities, averaged over the $0.1° \times 0.1°$ pixels used in our analysis, for a small region of the Stripe 82 area. The map is shown both before (left) and after (right) PSF correction, showing the effective removal of the PSF-induced ellipticities seen in particular along the top of the map on the left. For reference, a stick of ellipticity $e = 0.1$ is labeled at the top of each panel.

ξ_+ is simply equal to

$$\xi_+(\theta) = \int \frac{d^2l}{(2\pi)^2} C_l^{EE} \left[j_0(l_x\sigma/2) j_0(l_y\sigma/2) \right]^2 \cos\left[l_x\theta \right].$$ (6)

The goal is to separate modes produced by scalar cosmological perturbations (so-called E-modes) from those produced by systematics (B-modes). Several groups have shown (Schneider et al. 2002; Fu et al. 2008) that the cleanest way to do this is to define

$$\xi_{E,B}(\theta) = \frac{\xi_+(\theta) \pm \xi'(\theta)}{2}.$$ (7)

where

$$\xi'(\theta) \equiv \xi_-(\theta) + 4 \int_0^\infty \frac{dx}{x} \xi_-(x) \left(1 - 3\frac{\theta^2}{x^2} \right).$$ (8)

For scalar perturbations, $\xi_B = 0$, and $\xi_E = \xi_+$. To check for systematics, we will compute all of these but argue that ξ_+ may be slightly polluted by a small B-mode contamination so we obtain final cosmological constraints from ξ_E.

An alternative approach is to extract the C_l spectra directly from a quadratic estimator of the observed shears, essentially inverting Eq. (2) and its cousins. In §5, we describe algorithms for this direct approach of extracting the E- and B-spectra.

4. CORRELATION FUNCTION RESULTS

4.1. Simulations

To set up expectations, we generated mock catalogs of shear for the Stripe 82 area, first divided into 42 $2.6° \times 2.6°$ boxes, and then with each box further subdivided into square pixels of size $6' \times 6'$ $(= 0.1° \times 0.1°)$. The cosmic shear in each pixel is drawn from a Gaussian distribution with mean zero and covariance matrix that includes both signal and shape noise. The signal part of

the covariance matrix accounts for all correlations over the larger box and is computed using Eq. (2) and similar 2-point functions for γ_2 assuming a standard ΛCDM model ($H_0 = 70$ km s^{-1} Mpc^{-1}; $\Omega_m = 0.25$, $\sigma_8 = 0.8$) and the redshift distribution depicted in Fig. 1. Shape noise adds a diagonal term to the shear covariance matrix equal to $(e_{\rm int}/R)^2/N_i$, where the intrinsic shape noise $e_{\rm int} = 0.37$ and the shear responsivity $R = 1.7$, as noted earlier in Section 2.3. The number of galaxies N_i in the i-th small pixel is set equal to the number of galaxies in the real data in that same pixel with one caveat. The average density of galaxies per pixel in the mock catalog is 264, similar to the SDSS data set with no photo-z cuts. The density in the catalog with $\sigma_z < 0.15$ is more than a factor of two smaller than this. So the errors estimated using the mocks should be smaller than those we eventually obtain using the cut photo-z samples.

We generate 23 full Stripe 82 mock surveys, each of which is divided into 42 $2.6° \times 2.6°$ boxes, for a total of 966 boxes. For each of these boxes we compute the shear-shear correlation function vs. θ, the angular separation between the $0.1° \times 0.1°$ spatial pixels into which the simulated shears are binned. We first use the following estimator for the tangential (ξ_{tt}) and cross ($\xi_{\times\times}$) correlation functions

$$\xi_{tt}(\theta) = \frac{\sum_{i,j} N_i N_j \gamma_{t,i} \gamma_{t,j}}{\sum_{i,j} N_i N_j}$$ (9)

$$\xi_{\times\times}(\theta) = \frac{\sum_{i,j} N_i N_j \gamma_{\times,i} \gamma_{\times,j}}{\Sigma_{i,j} N_i N_j}$$

where the sum is over all pairs i, j of pixels separated by the angle θ, $\gamma_{t,i}$ and $\gamma_{\times,i}$ are the tangential and cross components of the shear in pixel i (related to the ellipticity by $\gamma = e/R$), and N_i is the number of galaxies in pixel i. The weighting by N_i is equivalent to inverse variance weighting according to the number of galaxies in
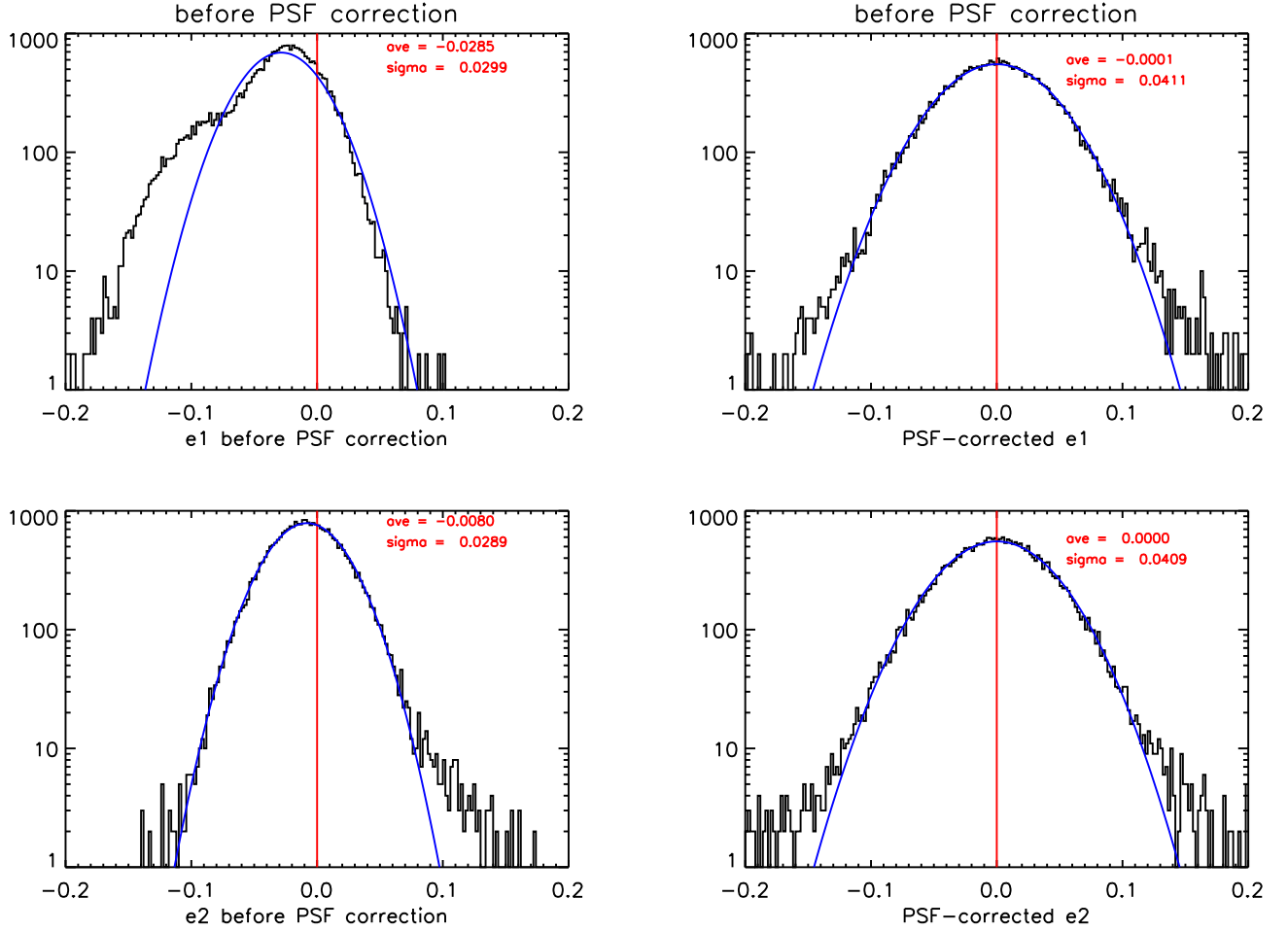
FIG. 4.— The distribution (black) of galaxy ellipticities e_1 (top) and e_2 (bottom), averaged over the $0.1° \times 0.1°$ pixels used in our analysis, for the photo-z error < 0.15 sample. The distributions are shown both before (left) and after (right) PSF correction, in order to demonstrate the effectiveness of our procedure in removing the PSF from the galaxy ellipticity measurements. Also shown are best-fit Gaussians (blue), which are good approximations to the PSF-corrected ellipticity distributions. The text in red gives the mean and σ of the Gaussian in each panel.
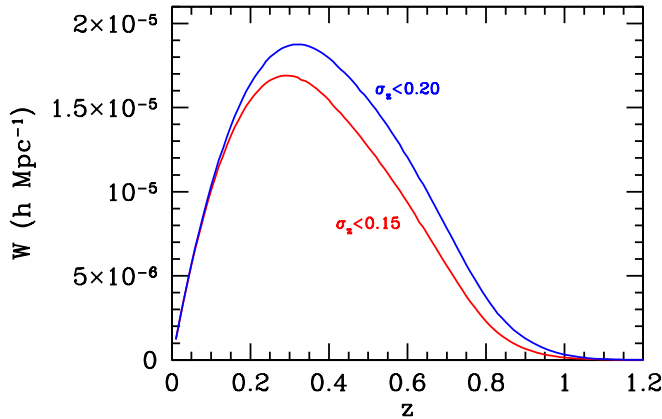
FIG. 5.— The window function that weights the power spectrum in Eq. (3) for background galaxies in the two cuts used in our sample.

each pixel, taking each mock galaxy to contribute a fixed amount of intrinsic shape noise $\sigma_\gamma = e_{\text{int}}/R$ per shear component. We then compute the ξ_+ correlation function using Eq. (5) and plot the results in Fig. 6, where

we show the mean (and standard deviation of the mean) of ξ_+ averaged over all the mock catalogs, as well as the results from a single, typical Stripe 82 mock. Also plotted as a curve is the input correlation function. At small θ, the mean value of ξ_+ averaged over all the mocks is slightly higher than the input ξ_+ due to binning. A given angular bin contains only a fixed number of separations because the pixel centers are spaced periodically. For example, the lowest bin, shown as centered on $\theta = 0.13°$, contains only the two separations $0.1°$ and $0.14°$. A proper treatment would weight these two contribution appropriately and eliminates the small discrepancy. However, this weighting produces only very small changes in ξ, changes that we are sensitive to only when considering the average over all the mocks, but which are far below the noise in the actual data set, as can be seen in Fig. 6.

We then extract cosmological parameters from each of the 23 mock surveys. To do this, we form a χ^2 with the covariance matrix measured from the 42 boxes comprising each Stripe 82 mock catalog. We then scan over a range of values of σ_8 and Ω_m, and Fig. 7 shows the resulting best-fit σ_8 and Ω_m values for all the mocks, along
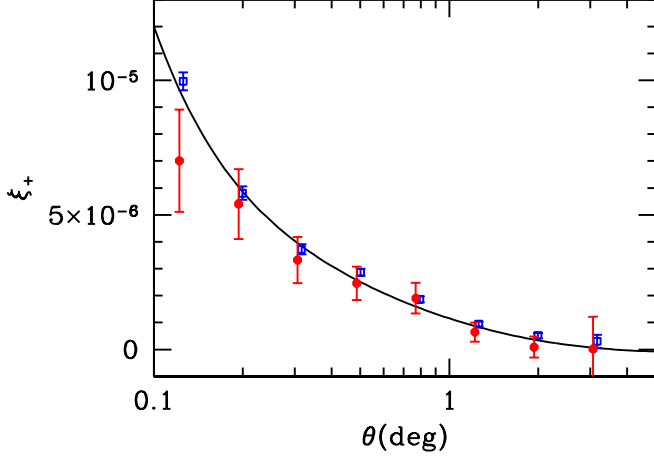
FIG. 6.— Correlation function ξ_+ measured for 23 mock catalogs, each consisting of the full Stripe 82 area. The solid curve is the input true correlction function. The rectangular open (blue) points and error bars show the mean and standard deviation of the mean of ξ_+ averaged over all 23 mocks, while the circular closed (red) points and errors are the results for a single, typical mock.
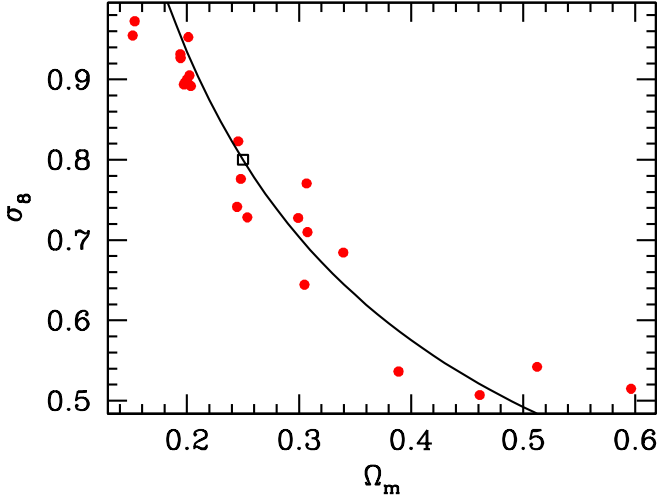
with the true values for the input model.

FIG. 7.— Best fit values of the cosmological parameters σ_8 and Ω_m from 23 mock catalogs, each simulating the full Stripe 82 area, analyzed with the correlation function. The open square denotes the true input model. The line traces out the degenerate direction, with $\Omega_m^{0.7}\sigma_8$ constant.

Fig. 7 suggests a convenient way to quote the results of both the mocks and the data. Apparently only a combination of the two parameters is constrained by the data, with the degeneracy given by $\Omega_m^{0.7}\sigma_8 = $ constant. The input value of this combination (with $\Omega_m = 0.25$ and $\sigma_8 = 0.8$) was $\Omega_m^{0.7}\sigma_8 = 0.303$, while the mean over all mocks was 0.300. The rms of the mocks was 0.022, consistent with the error bar from a single mock.

4.2. Data

We now compute the shear-shear correlation functions for the real data and plot them in Fig. 8. We use the same estimators for the tangential (ξ_{tt}) and cross ($\xi_{\times\times}$) correlation functions given earlier in Eq. (9). The weight-

ing is again inverse variance weighting according to the number of galaxies in each pixel, now taking each real galaxy to contribute a fixed amount of noise $\sigma_\gamma = \sigma_e/R$ per shear component. As noted earlier in Section 2.3, for our galaxies $\sigma_e = 0.45$ and includes both intrinsic shape noise and the ellipticity measurement error.

We then compute the ξ_+ correlation function using Eq. (5) and the E- and B-mode correlation functions via Eq. (7), and plot the results for these three correlation functions in Fig. 8, for each of our photo-z error < 0.15 and < 0.2 samples. As we did for the simulations, for the real data we also compute the correlation functions by first dividing the Stripe 82 area into 42 non-overlapping $2.6° \times 2.6°$ square boxes, then calculating ξ_+, ξ_E, and ξ_B separately for each box, and finally averaging the results over all the boxes. We use this procedure as it allows us to easily derive an empirical estimate of the uncertainties and the covariance matrix of the data, using the variances and covariances of the ξ values determined over the ensemble of 42 boxes. The correlation functions are computed in eight evenly spaced, logarithmic bins of pixel pair separation θ, ranging from $0.13°$ to $3.16°$.

The top panels of Fig. 8 show that we have a significant cosmic shear signal in our data on scales of about $0.1°$ to about $1.3°$. The bottom panels of Fig. 8 show that the individual $\xi_B(\theta)$ values are mostly consistent with zero within the error bars, though overall there does appear to be some small positive B-mode systematic in the data. This is consistent with the top panels of Fig. 8, which show that the ξ_E values are generally somewhat smaller than the ξ_+ values; recall from Eq. (7) that $\xi_+ = \xi_E + \xi_B$. For the case of no B-mode contamination, it should suffice to use the more robustly computed ξ_+ for cosmology fitting, but for our data we will consider both ξ_+ and ξ_E in the cosmology fits, in order to check for the impact of potential B-mode contamination. The best-fit results are also shown in Fig. 8 and will be discussed below in Section 6.

4.3. Systematics Check

Imperfect PSF corrections are the main source of systematics for cosmic shear measurements. We can verify that our systematics are under control by computing the cross-correlation between the corrected galaxy ellipticities e and the uncorrected stellar ellipticities $e^\star$, normalized by the auto-correlation of $e^\star$, following the procedure of Bacon et al. (2003). Here we do something similar, but use the PSF model ellipticities e_{PSF} evaluated at the location of each galaxy, instead of the measured ellipticities of a separate sample of stars. This serves the same purpose, i.e., to identify in the measured shear signal γ any spurious contributions due to uncorrected contamination from the PSF ellipticity. If the observed shear is contaminated by the PSF, then

$$\gamma = \gamma_{\mathrm{true}} + a\gamma_{\mathrm{PSF}} \; , \qquad (10)$$

where a is a constant. Then the observed two-point correlation function gets an unwanted contribution of

$$\xi_+^{\mathrm{SYS}} = a^2\langle\gamma_{\mathrm{PSF}}\gamma_{\mathrm{PSF}}\rangle. \qquad (11)$$

The constant a can be estimated by cross-correlating the PSF model ellipticities with the galaxy ellipticies leading to (Bacon et al. 2003)

$$\xi_+^{\mathrm{SYS}} = \frac{\langle\gamma\;\gamma_{\mathrm{PSF}}\rangle^2}{\langle\gamma_{\mathrm{PSF}}\gamma_{\mathrm{PSF}}\rangle} \; , \qquad (12)$$
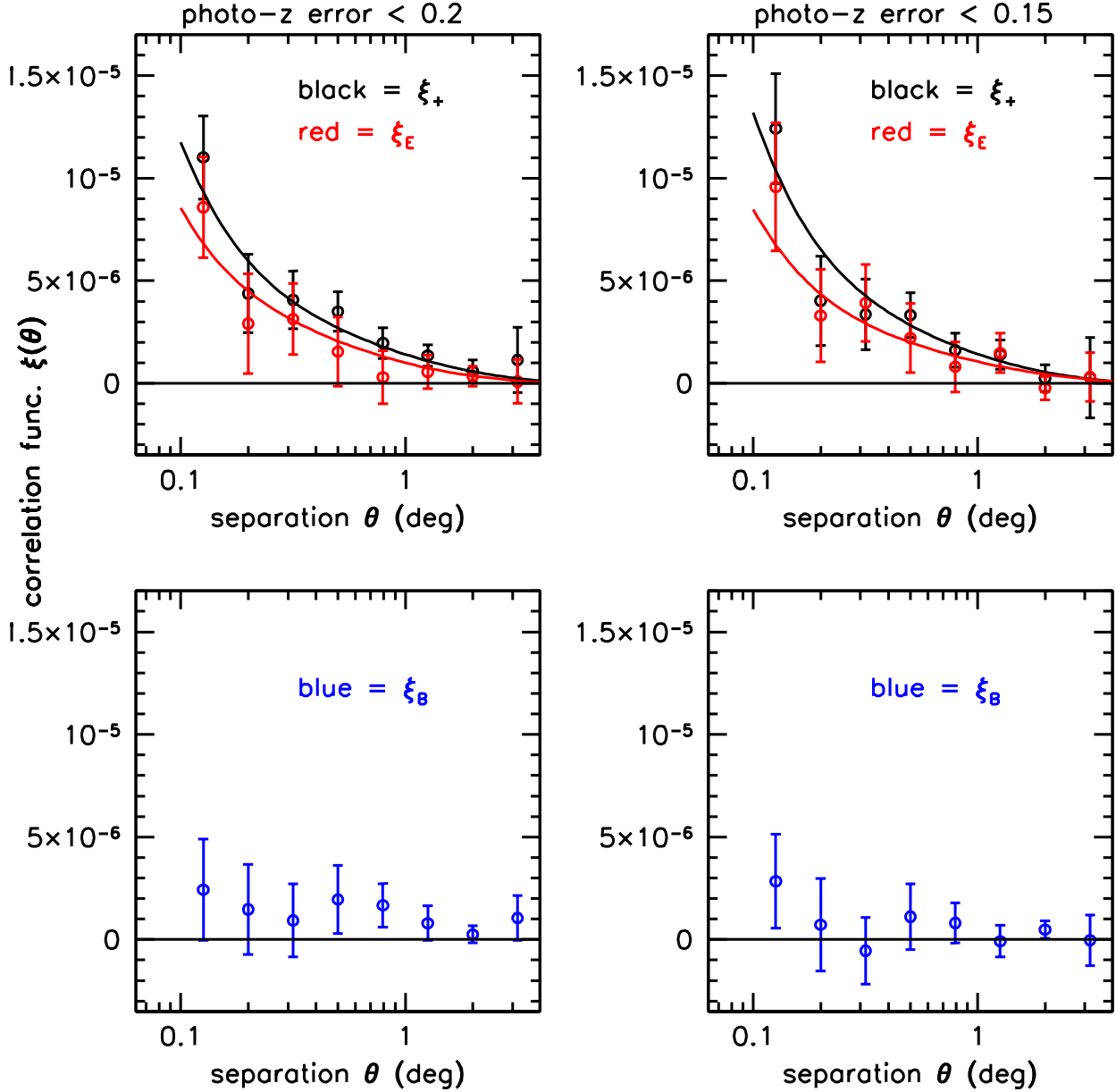
FIG. 8.— The measured shear-shear correlation functions for our data, plotted as data points with error bars, in logarithmically-spaced bins of angular separation θ. The results for ξ_+ (black) and ξ_E (red) are plotted in the top panels, and the results for ξ_B (blue) are shown in the bottom panels. Note the y-axis range is the same in the top and bottom panels to facilitate comparisons. The left-hand panels are for the photo-z error $\sigma_z < 0.2$ sample and the right-hand panels for the $\sigma_z < 0.15$ sample. The curves in the top panels are the correlation functions derived from the best-fitting cosmologies to each photo-z error sample, using either the ξ_+ or ξ_E data.

where the angular correlation function ξ_+^{SYS} can be directly compared to ξ_+, providing an estimate of the PSF systematic effect on our measurement. Error bars are computed for ξ_+^{SYS} the same way as for ξ_+, using the standard deviation of the mean values of ξ for the 42 boxes into which Stripe 82 is divided. Figure 9 shows the result of this check for both the $\sigma_z < 0.15$ and $\sigma_z < 0.2$ samples, demonstrating that our PSF systematics are at about the 1% level on scales $\theta < 2°$. For the two largest θ bins, ξ_+^{SYS} appears to be larger in proportion to ξ_+, but are still small compared to the larger ξ_+ errors on those scales. We have explicitly compared the cosmology fits

with and without first subtracting off ξ_+^{SYS} from ξ_+ and have found negligible differences, thus confirming that our cosmology results are not significantly contaminated by residual PSF systematic errors.

In addition to PSF-related systematics, uncertainties in the redshift distribution of our galaxy sample will also lead to errors in our cosmic shear results. As discussed earlier in Section 2.2, we address this issue by presenting our results using two galaxy samples defined by the different photo-z error cuts $\sigma_z < 0.2$ and $\sigma_z < 0.15$. As will be shown in Section 6, our cosmology results are insensitive to the choice of photo-z cut.
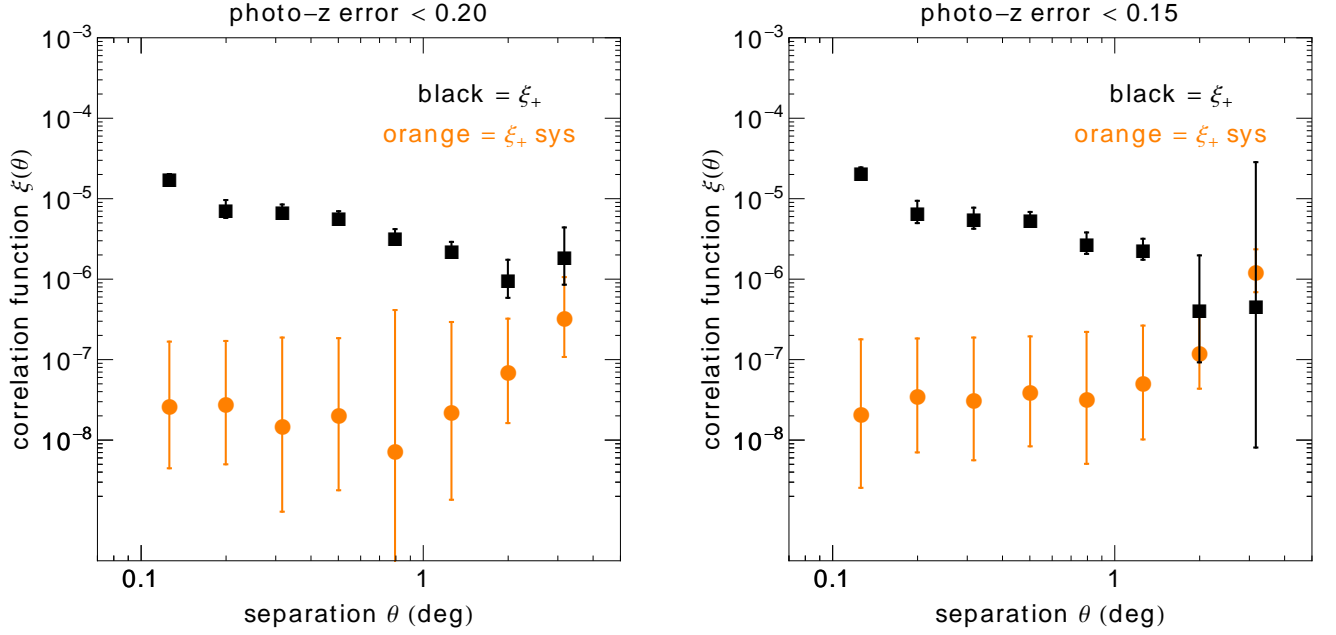
FIG. 9.— Comparison between the correlation function ξ_{+}^{SYS} induced by residual PSF systematics (orange) and the shear-shear correlation function ξ_{+} (black), for both the $\sigma_z < 0.20$ (left) and $\sigma_z < 0.15$ (right) samples, demonstrating that our PSF systematics are at a 1% level on scales $\theta < 2°$. See Section 4.3 for additional discussion.

Also, as described in Section 2.3, we found and corrected for a residual additive bias in the shear measurement, which is likely due to CCD camcol-dependent errors in the PSF model affecting the subsequent linear PSF correction and galaxy ellipticity measurements. In addition to this additive bias, the Hirata & Seljak (2003) linear PSF correction scheme we use is subject to a multiplicative shear calibration error $\delta\gamma/\gamma$ that depends on galaxy type and resolution factor. This issue was studied in detail for SDSS galaxies in Hirata & Seljak (2003) and Hirata et al. (2004), with the latter concluding that $|\delta\gamma/\gamma| \lesssim 0.07$. This fractional shear calibration error leads to a fractional error in the correlation function $|\delta\xi/\xi| \approx 2|\delta\gamma/\gamma| \lesssim 0.14$. Compared to the statistical fractional error in the amplitude of ξ_{+} of about 0.25 (determined as usual from our 42 boxes on Stripe 82), the additional systematic fractional uncertainty $|\delta\xi/\xi|$ due to shear calibration leads only to a $\lesssim 15\%$ increase in the fractional error on ξ_{+} when added in quadrature. We will neglect this as it is a small effect compared to the much larger existing statistical errors on ξ.

5. POWER SPECTRUM

The power spectrum and the correlation function are complementary ways of measuring the two point statistics of any field. The power spectrum method, however, has been used less commonly for cosmic shear (but see Brown et al. 2003), due to the complexity in accounting for the non-trivial window function in Fourier space that arises from survey geometry and from a non-uniform galaxy distribution. In this section we estimate the power spectrum of the Stripe 82 coadded data, while accounting for the effects of the survey geometry and of spatially non-uniform shape noise. We use the quadratic estimator (hereafter "QE") to estimate the power spectrum and its errors, following the approach proposed by Hu & White (2001) (also see Seljak 1998). To cross-check our answer, we also derive the power spectrum using a fast

Fourier transform, taking advantage of the nearly flat geometry of Stripe 82, and construct a pseudo estimator (hereafter "PE") of the power spectrum. For the pseudo estimator, we first weight the shear value measured in each pixel with the inverse shape noise in order to down-weight masked pixels or pixels with large shape noise, then Fourier transform, generate a pseudo power spectrum, and finally deconvolve the effect of the weight to extract an unbiased power spectrum. We test the fidelity of these methods using the 23 Gaussian SDSS mock catalogs that mimic the Stripe 82 data, and then apply the two methods to the observed real Stripe 82 data. In order to ease the computational load in calculating matrix operations, we divide the Stripe 82 data into 42 boxes of $2.6° \times 2.6°$ and ignore the correlations between different boxes. That is, we lose clustering information on scales larger than $\sim 1.3°$.

5.1. Quadratic Estimator

5.1.1. Summary of Method

We follow the method described in Hu & White (2001), which is summarized below. We first assume that the likelihood of the measured shear field is:

$$\mathcal{L} = \frac{1}{(2\pi)^N |\mathbb{C}(\mathcal{D}_\alpha)|^{1/2}} \exp\left[-\frac{1}{2} d^T \mathbb{C}^{-1}(\mathcal{D}_\alpha) d\right], \quad (13)$$

where d is the data vector, i.e., the two components of the measured shear field for the 42 boxes of 26×26 pixels. The covariance matrix $\mathbb{C}$ is the sum of the cosmological signal $\mathbb{C}^{\mathrm{sig}}$ and the noise $\mathbb{C}^{\mathrm{noise}}$ due to the rms intrinsic ellipticity and the measurement errors:

$$\mathbb{C} = \mathbb{C}^{\mathrm{sig}} + \mathcal{D}_N \mathbb{C}^{\mathrm{noise}}, \quad (14)$$

where we have inserted a parameter $\mathcal{D}_N$ to account for any deviation from the assumed level of shape noise; that is, if the shape noise is known perfectly, then $\mathcal{D}_N$ is fixed to one. In the case of data with large shape noise, we

find that $\mathcal{D}_N$ and the EE and BB power from the cosmic signal are difficult to estimate simultaneously, so we will fix $\mathcal{D}_N$ to unity. But it is useful to allow it to vary in the case of relatively low shape noise. Since we are ignoring the correlation between the boxes, $\mathbb{C}$ is block-diagonal, with 42 separate blocks. The signal part is identical from box to box, but because the galaxy density varies, the shape noise differs slightly from one block to another.

Labeling the shear components with indices a, b and the pixels with i, j, the covariance matrices are

$$\mathbb{C}^{\mathrm{sig}}_{(ij)(ab)} = \langle \gamma_a(\vec{n}_i)\gamma_b(\vec{n}_j)\rangle,$$

$$\mathbb{C}^{\mathrm{noise}}_{(ij)(ab)} = \frac{\sigma_\gamma^2}{N_i}\delta_{ij}\delta_{ab}, \qquad (15)$$

where N_i is the number of galaxies in pixel i and σ_γ is the rms of the shears of all the galaxies.

Eq. (2) gives the expression for one element of the signal covariance matrix under the assumption that only the E-mode is non-zero. We want to simultaneously measure the E- and B- modes (using the latter as a systematics check), so we need to generalize Eq. (2). Following Hu & White (2001), we write

$$\langle \gamma_1(\vec{n}_i)\gamma_1(\vec{n}_j)\rangle = \int \frac{d^2l}{(2\pi)^2}[C_{EE}(l)\cos^2 2\varphi_l$$

$$+C_{BB}(l)\sin^2 2\varphi_l - C_{EB}(l)\sin 4\varphi_l]W^2(\vec{l})e^{i\vec{l}\cdot(\vec{n}_i-\vec{n}_j)},$$

$$\langle \gamma_2(\vec{n}_i)\gamma_2(\vec{n}_j)\rangle = \int \frac{d^2l}{(2\pi)^2}[C_{EE}(l)\sin^2 2\varphi_l$$

$$+C_{BB}(l)\cos^2 2\varphi_l + C_{EB}(l)\sin 4\varphi_l]W^2(\vec{l})e^{i\vec{l}\cdot(\vec{n}_i-\vec{n}_j)},$$

$$\langle \gamma_1(\vec{n}_i)\gamma_2(\vec{n}_j)\rangle = \int \frac{d^2l}{(2\pi)^2}[\frac{1}{2}(C_{EE}(l) - C_{BB}(l))\sin 4\varphi_l$$

$$+C_{EB}(l)\cos 4\varphi_l]W^2(\vec{l})e^{i\vec{l}\cdot(\vec{n}_i-\vec{n}_j)}, \qquad (16)$$

where φ_l is the angle between $\vec{l}$ and the x-axis, $W(\vec{l}) = j_0(l_x\sigma/2)j_0(l_y\sigma/2)$ is the pixel window function in Fourier space, and σ is the pixel side $(0.1°)$ in radians.

We now approximate the angular power spectra with piecewise constant band powers; that is, we set $l(l+1)C(l)/2\pi$ to a constant value $\mathcal{D}_\alpha$ over a band α spanning a range of l. Then the signal covariance matrix is a linear combination of the band powers:

$$\mathbb{C}^{\mathrm{sig}}_{(ij)(ab)} = \sum_\alpha \mathcal{D}_\alpha \int_{l\in\alpha} \frac{dl}{2(l+1)}$$

$$\times \left[w_0(l)I^\alpha_{(ij),(ab)} + \frac{1}{2}w_4(l)Q^\alpha_{(ij),(ab)}\right], (17)$$

where $\mathcal{D}_\alpha$ are the EE, BB, and EB band powers. The integration in Eq. (17) runs over the range of l within each band. We refer readers to Hu & White (2001) for the exact forms of w_0 and w_4, which are the decomposed pixel window functions, and matrices $I^\alpha_{(ij),(ab)}$ and $Q^\alpha_{(ij),(ab)}$ [1].

By maximizing the likelihood as a function of the angular power spectrum, i.e., by finding $\mathbb{C}^{\mathrm{sig}}$ that describes the observed data the best, we derive the best-fit shear angular band powers. The solution is derived iteratively

---

[1] Hu & White (2001) has a typo in Eq. (14): $Q^{\beta\beta}$ for $\langle\gamma_2\gamma_2\rangle$ is $J_0 + 2c_4 J_4 + c_8 J_8$, not $J_0 + 2c_4 J_4 - c_8 J_8$.

by using the Newton-Raphson method to find the root of $d\mathcal{L}/d\mathcal{D}_\alpha = 0$, and each step toward an improved estimate is determined by stepping

$$\delta\mathcal{D}_\alpha \propto \sum_\beta \frac{1}{2}(F^{-1})_{\alpha\beta}\mathrm{tr}[(dd^T - \mathbb{C})(\mathbb{C}^{-1}\mathbb{C}_{,\beta}\mathbb{C}^{-1}], (18)$$

where $\mathbb{C}_{,\alpha} \equiv \partial\mathbb{C}/\partial\mathcal{D}_\alpha$ and the Fisher matrix is

$$F_{\alpha\beta} = \frac{1}{2}\mathrm{tr}(\mathbb{C}^{-1}\mathbb{C}_{,\alpha}\mathbb{C}^{-1}\mathbb{C}_{,\beta}). \qquad (19)$$

Assuming that the likelihood is sufficiently Gaussian near the maximum, we interpret F^{-1} as the covariance matrix of the measured band powers.

Given an estimated band power, how do we correct for the finite band width and compare it to the theoretical prediction? The simplest ideas – taking the value of $\mathcal{D}_\alpha$ at the center of the bin or averaging over all l's in the bin – are not quite right. Rather, each measured $\mathcal{D}_\alpha$ samples the C_l's with a window function of its own (see, e.g., Knox 1999) not exactly equal to a square well. To compute this, we use the fact that the expected value of the band power, $\langle\mathcal{D}_\alpha\rangle$, is related to the power spectrum at each wave number $\mathcal{D}(\ell')$ through the window function $\mathbb{W}_{\alpha\ell}$:

$$\langle p_\alpha \rangle = \sum_l \mathbb{W}_{\alpha\ell}\mathcal{D}_\ell, \qquad (20)$$

where ℓ is an integer wavenumber (taken here to lie within the range $10 < l < 3600$), and

$$\mathbb{W}_{\alpha\ell} = F^{-1}_{\alpha\beta}\frac{1}{2}\mathrm{tr}[\mathbb{C}^{-1}\mathbb{C}_{,\beta}\mathbb{C}^{-1}\mathbb{C}_{,\ell}], . \qquad (21)$$

Here $\mathbb{C}_{,\ell}$ is the derivative of $\mathbb{C}$ with respect to the power at an integer wavenumber ℓ and derived using Eq. (17) with $\Delta l = 1$, i.e., without integration. When we derive the cosmology fit, we convolve this window function with the theoretical model to compare to the data. Fig. 10 shows the window function for Stripe 82 for our bands. The right panel shows that indeed for the optimal quadratic estimator, our basic systematics test – absence of a B-mode – is robust, in that a model with only E-modes will *not* produce on average a spurious detection of B-modes due to the complicated geometry and non-uniform shape noise.

5.1.2. *Mock Tests*

We test our estimator using Gaussian mocks as described in §4. We analyze two sets of mock catalogs: one with very low shape noise and one with the pixel-to-pixel varying shape noise that is very similar to the observed data on Stripe 82. Hereafter we refer to the former as "low-noise mocks" and the latter as "SDSS mocks." The low-noise mock is generated using a theoretical Gaussian covariance matrix for the fiducial concordance cosmology, with a small amount of shape noise, i.e., $\sigma_\gamma^2/N_{\mathrm{gal}}$, with a constant $N_{\mathrm{gal}} = 250$ and $\sigma_\gamma^2 = 0.02176^2$; we generate one realization of the 42 boxes on Stripe 82.

We first use the low-noise mock to test our estimators in the case of minimal shape noise. Figure 11 shows the estimated band power (data points) and the associated errors for the EE and BB modes using the low-noise mock. The dashed line corresponds to the input cosmology. We find that the EE mode band power is consistent
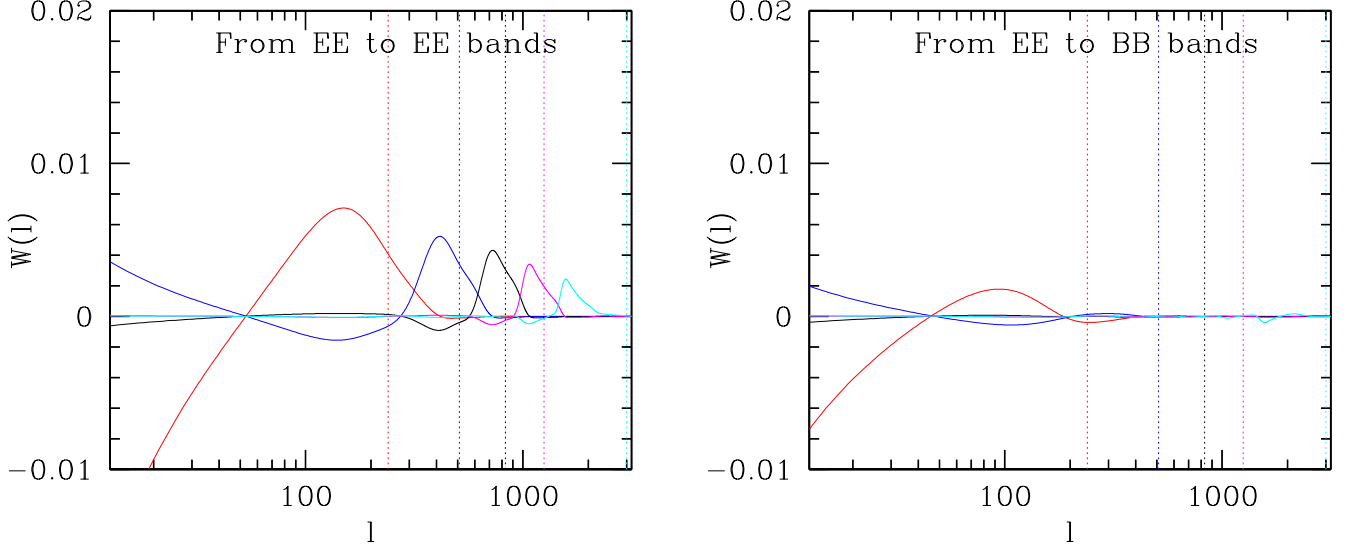
FIG. 10.— Band window functions. The left panel shows the contribution from the EE power spectrum at an integer wave number to the EE band power. The curves with different colors describe different bands and the vertical lines correspond to the naive centers of the bands. The sum of each curve is close to unity. The right panel shows the contribution from the EE power spectrum to the BB band power. As expected, there is no leakage between EE and BB modes on average.
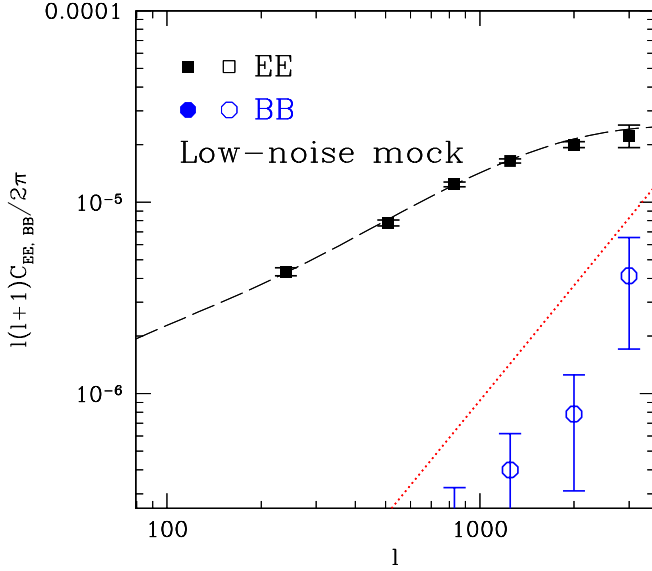

FIG. 11.— The best-fit EE (squares) and BB (circle) power spectra of the low-noise mock using the quadratic estimator without prior knowledge of the shape noise. A solid point denotes a positive value and an open point a negative value. The dashed line corresponds to the input cosmology. The error bars reflect the Gaussian error. The BB mode is much smaller than the EE mode and is zero within $1 - 2\sigma$. The dotted line shows the level of shape noise in the power spectrum.

FIG. 12.— Power spectra of the SDSS mocks using the quadratic estimator. Left: the average of the best-fit EE and BB power spectra of the 23 SDSS mocks. There are two sets of error bars. The larger set of error bars show the standard deviation among the 23 mocks. The smaller set of error bars show the error associated with the average of the 23 mocks, i.e., the standard deviation divided by $\sqrt{23}$. The dashed line shows the input EE power spectrum. The input BB power is zero. The red dotted line shows the shape noise contribution to the error on the band power.

with the input power spectrum to an impressive accuracy. The derived best fit BB power spectra are zero within $1 - 2\sigma$, i.e., fairly consistent with the input. We next test our methods in the presence of realistic

shape noise $\sigma_\gamma^2 = 0.25^2$, using $N_{\text{gal}}(\vec{x})$ similar to the real data, as described in §4. On average, these SDSS mocks

contain $N_{\rm gal} = 264$ per pixel. We have a total of 23 mocks of the 42 boxes.

Figure 12 shows the average and standard deviation of 23 SDSS mock power spectra derived using the quadratic estimator. We put two sets of error bars on each of the EE and BB band powers. The larger set of error bars corresponds to the error associated with one SDSS mock (i.e., the dispersion among the mocks), and the smaller set to the standard deviation divided by $\sqrt{23}$, i.e., the error associated with the average. Based on the larger set of error bars, one sees that we expect to recover the input power spectrum within 1σ for a survey comparable to Stripe 82. The dispersion among the mocks is consistent with the Gaussian error based on the inverse Fisher matrix to within 18%.

Fig. 13 shows the best-fit values of the cosmological parameters extracted from each mock. As in Fig. 7, the range of values is consistent with the input model, with an average $\Omega_m^{0.7}\sigma_8 = 0.303$, the same as the true input value. The rms value over all the mocks is 0.022 and is consistent with the 1σ error bars assigned to the parameter in a typical mock.
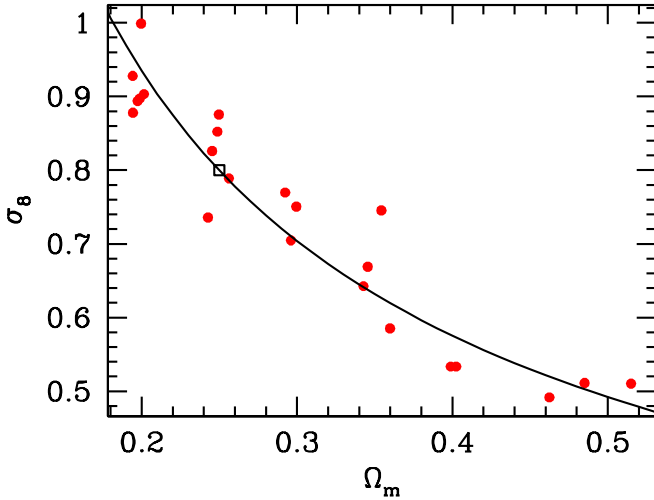
FIG. 13.— Best fit values of the cosmological parameters extracted from the C_l's of 23 mock catalogs (similar to Fig. 7 for ξ).

5.1.3. Data

We next apply this method to the real Stripe 82 data. Figure 14 shows the resulting QE power spectra for EE (left) and BB (right) modes for $\sigma_z < 0.15$ (top panels) and $\sigma_z < 0.2$ (middle panels), in comparison to the case with no σ_z cut in the bottom panels ("All" case in Figure 1). The case with no σ_z cut has the smallest shape noise ($N_{\rm gal} = 254/(0.1°)^2$) and is the most similar to the level of shape noise in the SDSS mocks (i.e., $N_{\rm gal} = 264/(0.1°)^2$). We detect strong EE-mode power with relatively negligible BB mode in this case, when the shape noise parameter is allowed to vary. Unfortunately, this case is not useful for deriving cosmological parameters, as we do not know the redshift distribution of the source galaxies (i.e., signal) accurately enough.

For the cases with $\sigma_z < 0.15$ and $\sigma_z < 0.2$, the shape noise is much larger (129 and $163/(0.1°)^2$, respectively).

To decrease the degrees of freedom in accordance with the larger noise level, we either fix the BB mode to zero or fix the shape noise using the measured rms fluctuations in shear. We adopt the latter as our main result. Letting both vary simultaneously does not produce robust constraints with this noisy data set.

The top and the middle panels of Figure 14 show the QE power spectra when the rms shape noise for each component of the shear is fixed to be 0.262 and 0.275, respectively. Note that the resulting BB mode is consistent with zero for most of the bands. Meanwhile, the band beyond $l > 1000$ is systematically low compared to the small-scale clustering we expect for a reasonable range of concordance cosmologies. The error bar is so large though that including this band in the final fits does not change the parameter extraction. For each of the measured power spectra, the solid line is the best-fit, flat ΛCDM cosmology that will be presented in Section 6. The red dotted line shows a rough estimate of the contribution of the shape noise to the error on the band power; it is close to, but smaller than the measured power. If we fix the BB mode to zero, instead of fixing the shape noise, we find similar results. In detail, for $\sigma_z < 0.15$, the band power is slightly lower when we fix the BB mode to zero, a sign that the true shape noise level probably is slightly higher (by 1%) than $\sigma_\gamma^2 = 0.262$ that we assumed. For $\sigma_z < 0.2$, we find almost identical results for both treatments.

5.2. Pseudo Estimator

We next use the pseudo estimator to derive band powers and cross-check the band power measurement derived using the quadratic estimator.

5.2.1. Method

Given the long and thin survey geometry of Stripe 82, one can make a flat-sky approximation and, in an ideal case, compute a discrete Fourier Transform to derive the power spectrum. A complication arises because of the incomplete coverage of the survey area and the non-uniform sampling densities. Without any treatment, the shape noise contribution in the power spectrum is derived from $\int d\vec{x}\frac{\sigma_\gamma^2}{N_i}$ rather than $\frac{\sigma_\gamma^2}{\bar{N}}$, where N_i is the number of galaxies for the ith pixel and $\bar{N}$ is the average number of galaxies. It is apparent that pixels with zero galaxies will make the shape noise estimation difficult in the non-uniform sampling case. In order to resolve this issue, we design a pseudo power estimator that weighs the shear values in each pixel by the number of galaxies in that pixel, i.e., by inverse variance:

$$\tilde{\gamma} \equiv \frac{N_i\gamma}{\bar{N}}. \qquad (22)$$

Then this makes the shape noise contribution to the power spectrum be simply $\frac{\sigma_\gamma^2}{\bar{N}}$.

Meanwhile, such a weighting results in a convolution of power in Fourier space and therefore in mode-mixing between E- and B-modes. That is, the estimator is biased relative to the true power spectrum and also it is not an optimal estimator. In order to derive an unbiased estimate of the true power spectrum from the pseudo power spectrum, we need to construct the mode-coupling matrix based on the number weighting scheme we used and
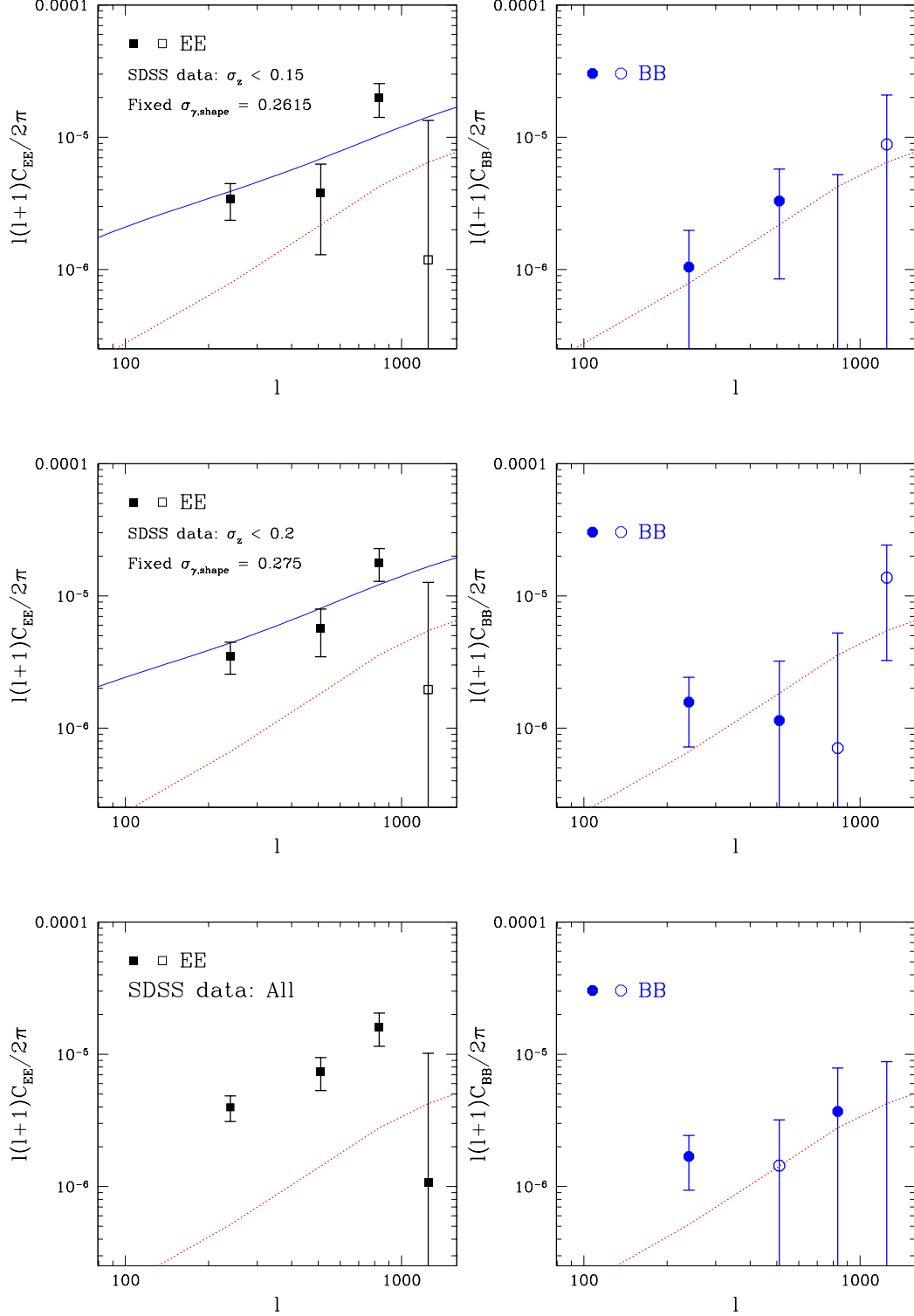
FIG. 14.— Estimates of the EE (left) and BB (right) power spectra for the SDSS Stripe 82 data with $|e_1|, |e_2| < 1.4$. The top panels show the case with $\sigma_z < 0.15$, and the middle panels show the case with $\sigma_z < 0.2$. The bottom panels show the case with no σ_z cut. The first two cases have quite high shape noise contributions. To decrease the number of degrees of freedom, we derive band powers while fixing the shape noise to be the measured rms fluctuations in shear: $\sigma_\gamma^2 = 0.262$ and 0.275, respectively. The solid lines show the best-fit cosmologies for these two cases. The red dotted lines show the level of the shape noise contribution to the error on the band power. As a comparison, the bottom panels for the no σ_z cut case show the band power derived while the shape noise is allowed to vary. While the EE band power is derived with a higher significance, the uncertainty in the redshift distribution of the source galaxies make this case difficult to interpret.
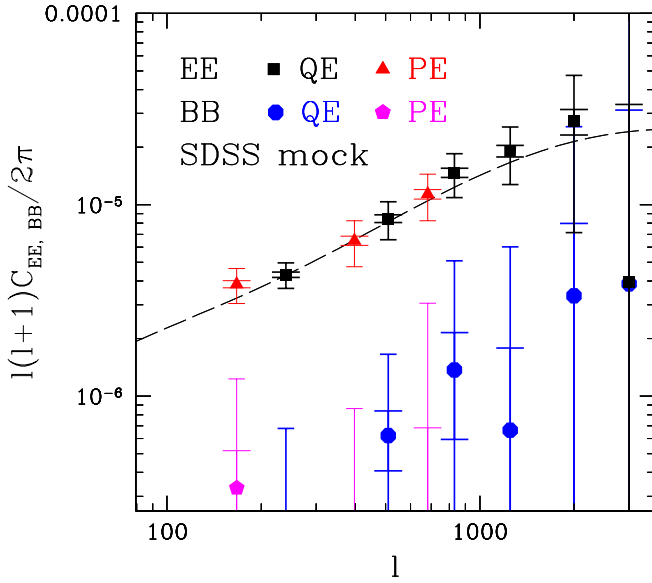
FIG. 15.— Average power spectra of the 23 SDSS mocks using the pseudo estimator (PE) in comparison with the quadratic estimator (QE). There are two sets of error bars. The larger set of error bars show the standard deviation among the 23 mocks. The smaller set of error bars show the error associated with the average of the 23 mocks, i.e., the standard deviation divided by $\sqrt{23}$. The dashed line shows the input EE power spectrum. The input BB power is zero.

deconvolve it by matrix inversion. Hikage et al. (2011) have shown the procedure for deriving the unbiased estimate of the true power spectrum from the pseudo power spectrum in the presence of a survey masking effect. Our case is analogous to theirs except that our pseudo power spectrum includes the effect of the number weighting scheme rather than the masking effect. We therefore follow the deconvolution procedure in Hikage et al. (2011) to remove the mode-coupling effect due to the weighting as well as the finite sky effect. We refer readers to Hikage et al. (2011) for further details for setting up these matrix operations.

5.3. *Pseudo Estimator vs. Quadratic Estimator*

In Figure 15, we show the average and standard deviation of 23 SDSS mock power spectra derived using the pseudo estimator (red triangles for E-mode and magenta pentagons for B-mode) in comparison with the quadratic estimator (black squares for E and blue circles for B-mode). For the pseudo estimator, we use the input *rms* shape noise to subtract off the shape noise contribution. We cut off $l > 1000$ for the pseudo estimator: our pixel resolution causes a non-zero aliasing of power from smaller scales onto this scale. We observe a sign of deviation from the input power spectrum in the E-mode of the pseudo estimator at $l \sim 160$, but overall the results between the pseudo estimator and the quadratic estimator appear quite consistent.

We next apply the pseudo estimator to the Stripe 82 data. We again assume $\sigma_\gamma^2 = 0.262$ and 0.275, respectively, for each of the two data sets with $\sigma_z < 0.15$ and $\sigma_z < 0.2$. The error bars are derived by regenerating SDSS mocks using the sampling density distribution and

σ_γ^2 of each of the two data sets and by taking the dispersion among the 23 mocks. Figure 16 shows the resulting band power of the Stripe 82 data using the pseudo estimator, in comparison to the quadratic estimator. Overall we find consistency between the two estimators.

6. CONSTRAINTS ON COSMOLOGICAL PARAMETERS

The cosmic shear measurements described above are most sensitive to the power on scales of $10 - 60'$ or $l \sim 100 - 800$. This power is sensitive primarily to the amplitude of the fluctuations σ_8 and the matter density Ω_m; Fig. 17 displays the sensitivity to σ_8 for fixed Ω_m.

The theoretical predictions are obtained by convolving the nonlinear power spectrum in Eq. (3) with the window function describing the galaxy distribution, as plotted in Fig. 5. We approximate the nonlinear spectrum as a function of k and z using `halofit` (Smith et al. 2003). Recent work (Eifler 2010) has shown that `halofit` underpredicts the power spectrum by 6-7% on the scales of interest, compared with accurately calibrated simulations (Lawrence et al. 2010). Our implementation of `halofit` also differs from the simulations at about the same level at $z = 0$, but fortuitously agrees with them to within a few percent on the scales and redshifts probed by the Stripe 82 data. The systematic error on the cosmological parameters due to this theoretical uncertainty then should be at most 3% (since the power spectrum scales roughly as the square of σ_8) and is probably far below that. It is much smaller than the statistical uncertainty.

A final check is to compare the constraints in parameter space from the different data sets ($\sigma_z < 0.15, 0.20$) and techniques (C_l, ξ_+, ξ_E). It is simplest to compare the constraints on a single parameter, instead of in the 2D (σ_8, Ω_m) plane. As shown in Fig. 7, the data are most sensitive to the combination $\Omega_m^{0.7}\sigma_8$; Fig. 18 shows the constraints on this combination for the different ways of analyzing the data. The different cuts and techniques lead to consistent constraints. We also note that our best-fit $\chi^2 = 6$ using the ξ data for the $\sigma_z < 0.15$ sample, while $\chi^2 = 35$ assuming no signal ($\xi = 0$); the resulting $\Delta\chi^2 = 29$, indicating 5-σ detection of the cosmic shear signal in our data.

For our final constraints, we choose the most conservative cut, the data set with $\sigma_z < 0.15$, using ξ_E, which is un-contaminated by the B-modes. Fig. 19 shows our results in the Ω_m, σ_8 plane. The 1-σ range on the constrained parameter is

$$\Omega_m^{0.7}\sigma_8 = 0.252^{+0.032}_{-0.052}. \qquad (23)$$

The error bars are consistent with those obtained with the mock catalogs, accounting for the lower galaxy density in the sample with the photo-z cuts.

Fig. 19 shows the constraints in the 2D plane along with the constraints from the WMAP 7-year data (Komatsu et al. 2011). The two data sets give consistent results, and the complementarity tightens the constraints on Ω_m at the high end.

7. CONCLUSIONS

We have performed a cosmic shear analysis of the SDSS coadd data (Annis et al. 2011), a 275 square degree area
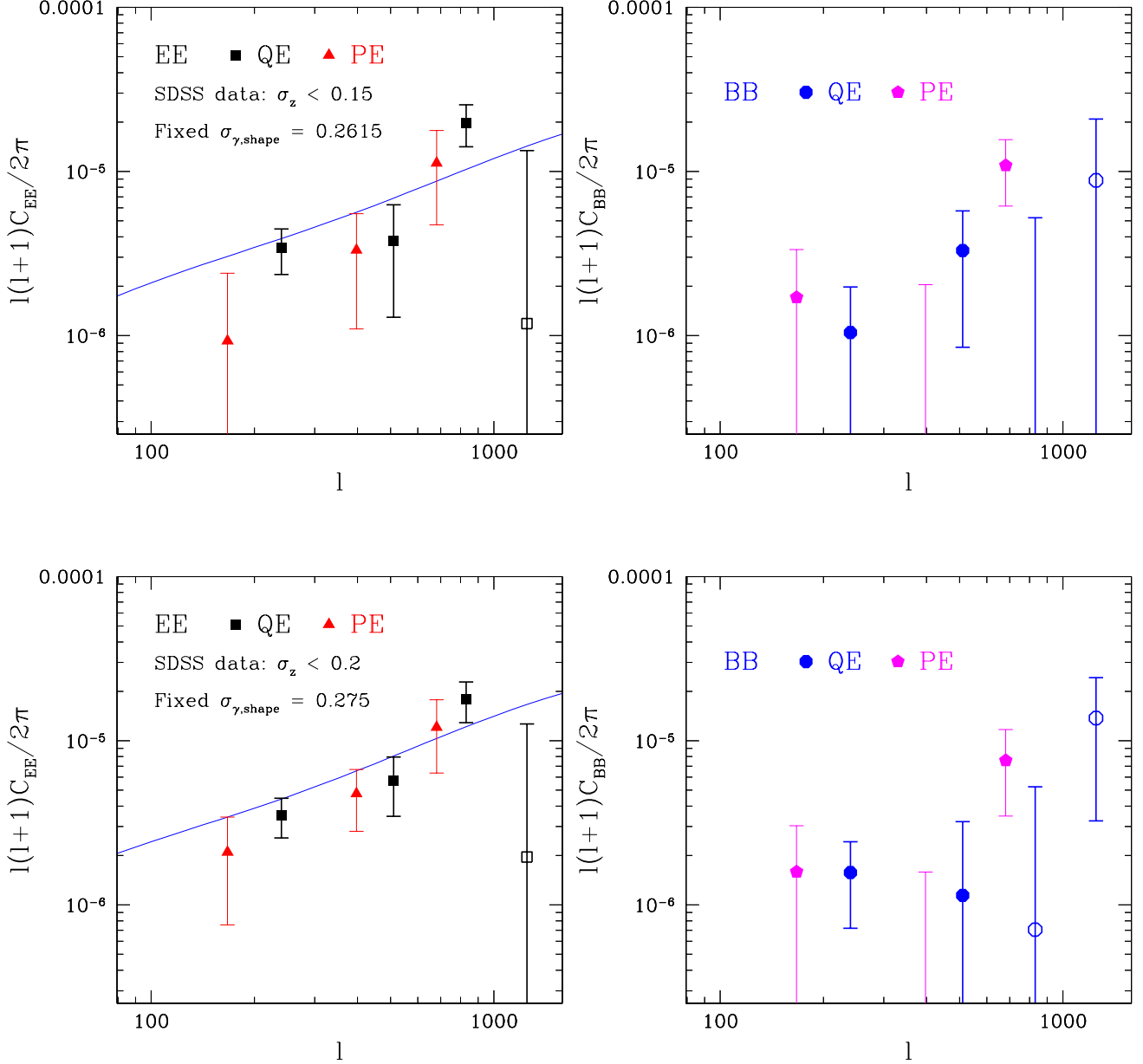
FIG. 16.— Estimates of the pseudo EE (left) and BB (right) power spectra for the SDSS Stripe 82 data (red triangles for E-mode and magenta pentagons for B-mode). We also plot the results of the quadratic estimator for comparison (black squares for E and blue circles for B-mode). The solid blue line shows the best-fit cosmology to the quadratic estimator. We find an overall consistency between the two estimators.

of the SDSS imaging data where we achieve 2 magnitudes fainter than the nominal depth of the survey through the coaddition of multiple exposures. Photometric redshifts for the coadd galaxies were obtained from their colors using a neural network algorithm (Reis et al. 2011) and corrections to the PSF modeling for accurate galaxy shape measurements were implemented as part of this work (Section 2).

Through a $> 5\sigma$ detection of the cosmic shear signal in the SDSS coadd data, we have measured the combination of the matter density Ω_m and the amplitude of matter fluctuations σ_8 in the Universe. The measurement was performed using both the shear-shear angular correlation function in real space (Section 4) and the power spectrum

in Fourier space (Section 5). We tested the quadratic estimator introduced by Hu & White (2001) for the power spectrum, plus our own version of the pseudo estimator; such power spectrum methods have not been commonly used in previous cosmic shear analyses of real data. Our power spectrum results are consistent with each other and with our correlation function results (Fig. 18). Our cosmological parameter constraint may be expressed as $\Omega_m^{0.7}\sigma_8 = 0.252^{+0.032}_{-0.052}$, which is in good agreement with WMAP (Fig. 19), as well as with other recent weak lensing surveys, in particular the next two largest area samples, CFHTLS (Fu et al. 2008, at 57 deg^2) and CTIO (Jarvis et al. 2003, at 75 deg^2), plus the much deeper COSMOS data set (Schrabback et al. 2010).
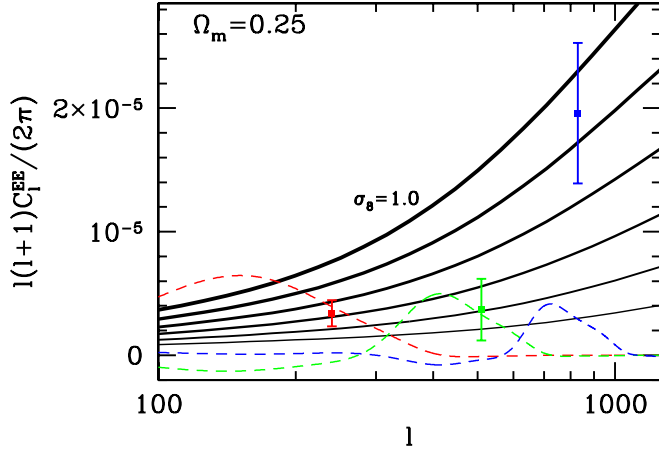
Fig. 17.— The power spectrum of the convergence, the EE spectrum, for different values of σ_8 and fixed Ω_m together with the data from §5 ($\sigma_z < 0.15$). Each (colored) data point is shown at the central value of its l-band. The result, though, can be interpreted only with the aid of the window function (dashed curves; unnormalized here), so, e.g., the band centered at $l = 240$ is actually most sensitive to power at $l \sim 170$.
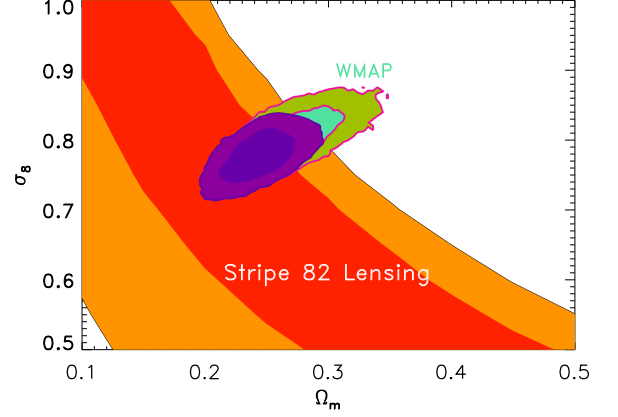

Fig. 19.— Constraints on cosmological parameters from SDSS Stripe 82 cosmic shear at the 1- and 2-σ level. Also shown are the constraints from WMAP. The innermost region is the combined constraint from both WMAP and Stripe 82.
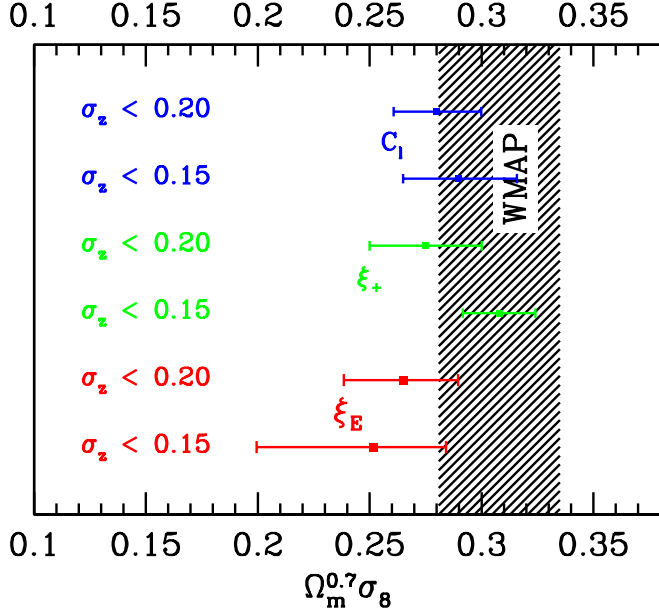
Fig. 18.— 68% Confidence levels on the parameter $\Omega_m^{0.7}\sigma_8$ from the different data sets and analysis techniques. Also shown is the 1-σ band from WMAP (Larson et al. 2011).

We have shown that the systematic effects on the correlation function due to PSF mis-modeling in our data are at the sub-percent level for scales up to 2°. We also tested samples with different photometric redshift error cuts. The most conservative σ_z cuts result in slightly better agreement among the different methods, indicating a minor effect and confirming the assumption that accurate photo-z estimates are crucial for cosmic shear studies.

Our 275 deg^2 Stripe 82 coadd data is the largest area survey for which cosmic shear has been measured, and our results pose an important precedent for future analyses of even larger area surveys, such as the Dark Energy Survey and LSST.

REFERENCES

Abazajian, K. N. et al. 2009, ApJS, 182, 543
Abbott, T., et al. 2005, arXiv:astro-ph/0510346
Abell, P., et al. 2009, arXiv:0912.0201
Annis, J., et al. 2011, arXiv:1111.6619
Bacon, D. J., Massey, R. J., Refregier, A. R., & Ellis, R. S. 2003, MNRAS, 344, 673
Bacon, D. J., Refregier, A. R., & Ellis, R. S. 2000, MNRAS, 318, 625
Bernstein, G. M., & Jarvis, M. 2002, AJ, 123, 583
Brown, M. L., et al. 2003, MNRAS, 341, 100
Drinkwater, M. J., et al. 2010, MNRAS, 401, 1429
Eifler, T. 2010, arXiv:1012.2978
Fu, L., et al. 2008, A&A, 479, 9
Fukugita, M., et al. 1996, AJ, 111, 1748
Garilli, B. et al. 2008, A&A, 486, 683
Gunn, J. E. et al. 1998, AJ, 116, 3040
Hamana, T., et al. 2003, ApJ, 597, 98
Heymans, C., et al. 2004, MNRAS, 347, 895
Hikage, C., Takada, M., Hamana, T., & Spergel, D. 2011, MNRAS, 412, 65
Hirata, C., & Seljak, U. 2003, MNRAS, 343, 459
Hirata, C. M. et al. 2004, MNRAS, 353, 529
Hoekstra, H., Yee, H. K. C., & Gladders, M. D. 2002, ApJ, 577, 595
Hu, W., & White, M. J. 2001, ApJ, 554, 67
Huff, E. M., et al. 2011, arXiv:1112.3143
Jarvis, M., et al. 2003, AJ, 125, 1014

Knox, L. 1999, Phys.Rev., D60, 103516
Komatsu, E. et al. 2011, ApJS, 192, 18
Larson, D., et al. 2011, ApJS, 192, 16
Lawrence, E., et al. 2010, ApJ, 713, 1322
Lupton, R., et al. 2001, ASP Conf. Series, 238, 269
Mandelbaum, R. et al. 2005, MNRAS, 361, 1287
Munshi, D., Valageas, P., van Waerbeke, L., & Heavens, A. 2008, Phys. Rep., 462, 67
Oyaizu, H., et al. 2008a, ApJ, 674, 768
—. 2008b, ApJ, 689, 709
Reis, R., et al. 2011, ApJ, submitted, arXiv:1111.6620
Rhodes, J., Refregier, A., & Groth, E. J. 2001, ApJ, 552, L85
Rhodes, J., et al. 2004, ApJ, 605, 29
Schneider, P., Van Waerbeke, L., & Mellier, Y. 2002, A&A, 389, 729
Schrabback, T., et al. 2010, A&A, 516, A63
Seljak, U. 1998, ApJ, 506, 64
Smith, R. E., et al. 2003, MNRAS, 341, 1311
Stoughton, C. et al. 2002, AJ, 123, 485
Van Waerbeke, L., et al. 2000, A&A, 358, 30
—. 2001, A&A, 374, 757
Weiner, B. J., et al. 2005, ApJ, 620, 595
Wittman, D. M., et al. 2000, Nature, 405, 143
Yee, H. K. C., et al. 2000, ApJS, 129, 475
York, D. G. et al. 2000, AJ, 120, 1579